Microstructure and corrosion study of Fe-based bulk metallic glass obtained by spark plasma sintering

L. Zarazúa-Villalobos, Nicolas Mary, J. Soo-Hyun, Kazuhiro Ogawa, Hidemi Kato, Yuji Ichikawa

L. Zarazúa-Villalobos, N. Mary, J. Soo-Hyun, K. Ogawa, H. Kato, Y. Ichikawa, Microstructure and corrosion study of Fe-based bulk metallic glass obtained by spark plasma sintering, Journal of Alloys and Compounds, Volume 880, 2021, 160399, ISSN 0925-8388,

Microstructure and corrosion study of Fe-based bulk metallic glass obtained by Spark Plasma Sintering

L. Zarazúa-Villalobos [a, b], N. Mary [b], J. Soo-Hyun [c, d], K. Ogawa [a, b], H. Kato [c], Y. Ichikawa [a]

a. Fracture and Reliability Research Institute (FRI), Tohoku University, 6-6-11-720, Aoba, Aramaki, 980-8579, Japan.
b. ELyTMaX, UMI 3757, CNRS, Tohoku University and Université de Lyon, International Joint Unit, Tohoku University, Japan.

c. Institute for Materials Research, Tohoku University (IMR) 2-1-1 Katahira, Aoba-ku, Sendai 980-8577, Japan.

d. Department of Materials Science and Engineering, Dankook University 119, Dandae-ro, Dongnam-gu, Cheonan-si, Chungcheongnam-do, 31116, Korea.

Abstract

Due to the necessity of developing new materials with better anti-corrosive properties, bulk metallic glasses are the focus of many research projects. In this study, a metallic glass with $Fe_{48}Cr_{15}Mo_{14}C_{15}B_6Y_2$ composition was produced by high-pressure atomization spray and densified by Spark Plasma Sintering. Different sintering cycles, temperatures, and pressures were carried out to conserve the amorphous structure while increasing its density. The temperatures used for this study were below the glass transition temperature, and the uniaxial force was variated between 50 to 400 MPa. Amorphous samples with nearly 98 % of relative density were obtained. The effect of the sintering cycle used on the phase transformation and microstructure of the materials was studied. Additionally, the porosity and crystallinity were related to the corrosion resistance properties through electrochemical characterization.

Key Words: Spark plasma sintering; Metallic glass; Corrosion resistance.

https://doi.org/10.1016/j.jallcom.2021.160399.

L. Zarazúa-Villalobos, N. Mary, J. Soo-Hyun, K. Ogawa, H. Kato, Y. Ichikawa, Microstructure and corrosion study of Fe-based bulk metallic glass obtained by spark plasma sintering, Journal of Alloys and Compounds, Volume 880, 2021, 160399, ISSN 0925-8388,

1. Introduction

Metallic glasses are increasing interest in academic researches and industry. They are electronically and optically like ordinary metals, but the absence of crystals and defects as vacancies, dislocations, or grain boundaries increase their chemical, physical and mechanical properties [1]. These materials could be used in a wide range of fields. They can be used to develop magnetic devices, microsystems, or for aeronautical or biomedical applications. The absence of grain boundaries provides high mechanical strength and corrosion resistance, making these materials an ideal candidate to stand up to aggressive environments depending on their composition [2–4].

Metallic glasses have been developed as powders, ribbons, and small pieces [2,3,5,6]. Coatings of metallic glass have also been studied by different deposition techniques [7–9]. However, new processing techniques that allow manufacturing larger pieces of bulk metallic glasses (BMGs) are still needed. Spark plasma sintering (SPS) is an advanced sintering technique for consolidating powders into nanostructured bulk materials. It has been recently used in broader applications and has gained a strong reputation as a versatile method for solid-state processing of metals, ceramics, and composites. The ease in parameter manipulation in SPS makes this process beneficial for the preservation of amorphous structures. [10]. Some studies have been performed to study the use of SPS in metallic glass processing [11,12]. They found that SPS can increase the specimens' size produced by a conventional copper mold casting in diameter and with a higher fracture strength.

https://doi.org/10.1016/j.jallcom.2021.160399.

One of the challenges to fabric BMG is to keep the amorphous structure on the materials. However, still unresolved if fully dense materials with some crystallinity percentage have higher corrosion resistance than a completely amorphous one with lower density.

Among the variety of BMGs, Fe-Cr-based bulk metallic glasses have attracted much attention because of superior corrosion resistance, high strength, and hardness. Like stainless steel, a concentration of Cr above 8 at.% leads to the growth of a passive film that protects the material from aggressive environments [13–15]. However, Fe-Cr-based BMGs exhibit almost no plastic strain and strain hardening even in compression when tested at room temperature, restricting their applicability [16]. In this study, SPS's effects on the densification, crystallinity, porosity, and corrosion properties of a Fe-Cr-Mo-C-B-Y metallic glass alloy are investigated to guide future SPS developments of Fe-Cr bulk metallic glasses.

2. Experimental

2.1. Metallic glass powder preparation

The appropriated amounts of high purity elemental materials (> 99.9 %) were used to produce the mother alloy with a final atomic composition of $Fe_{48}Cr_{15}Mo_{14}C_{15}B_6Y_2$. The 2 at.% of yttrium was added to the metallic composition because it enhanced the glass-forming ability [17,18]. The alloy was home-made by convection melting under an argon atmosphere, and the metallic glass powder was obtained by high-pressure spray atomization. After atomization, the powder was sieved until 43 μm mesh.

2.2 Spark Plasma Sintering parameters and characterization

https://doi.org/10.1016/j.jallcom.2021.160399.

Three different sintering cycles were selected to vary the samples' density while searching to conserve the amorphous phase. The first sintering cycle (S1) used a heating rate of 50 ℃/min until the final temperature (Tf) with 15 minutes of holding time at this temperature. Cycle two (S2) used an initial heating rate of 50 ℃/min until Tf-15 ℃ and a heating rate of 1℃/min until Tf. Cycle 3 (S3) used an initial heating rate of 50 ℃/min until Tf-30 ℃ and a heating rate of 1°/min until Tf.

The tests were performed in a commercial SPS (Fuji-SPS, japan) equipment using 7 g of powder, a tungsten carbide died of 15 mm of diameter, and Grafoil® as a protective film between the died and the powder. The final temperature was fixed at 575 °C, below the glass transition temperature (Tg) of this alloy (577 °C); the uniaxial force used for the test was 50 MPa. It worth mentioning that the Tg of this alloy was measured at a heating rate of 10 °C/min and the heating rate during the sintering process starts at 50 °C/min, which causes an increase in the Tg according to the works of T. Paul et al. [19,20].

The samples obtained by the three different sintering cycles were analyzed by XRD, SEM, and the density was measured by the Archimedes method. After the results of the three different sintering cycles were obtained, the one with better properties respecting the amorphous phase of the material was selected and used for the subsequent tests where the temperature and the uniaxial force were variated. All the samples obtained were analyzed by X-ray diffraction (XRD), and their densities were measured as well by the Archimedes' method. Table 1 reports the sample names and the SPS pressure and temperature used in this work. Note that the parameter selection is explained later in the document.

https://doi.org/10.1016/j.jallcom.2021.160399.

93 *2.3 Electrochemical test*

94 The electrochemical tests were performed in the samples obtained from the three different
95 sintering processes and the sample obtained after the variables' optimization. Before the test,
96 the samples' surface was polished until SiC 1200, and the roughness was measured by a 2D
97 profilometer using the JIS1994 standard in a Surfcoder SE300 (Kosaka Lab, Japan). Average
98 values were given for three profiles.

99 The electrochemical characterizations were carried out in a typical three-electrode glass cell.
100 The working electrode was the sample with an average surface of 1.10 cm^2 in contact with
101 the solution. The real surfaces were determined by optical surface measurements (Keyence
102 One Shoot microscope) before corrosion tests. A graphite rod (5 cm^2) and a Mercury Sulfate
103 Electrode (MSE, $0V_{MSE} = +0.650\ V_{ENH}$) were used as a counter electrode and the reference
104 electrode, respectively. Corrosion tests were performed in a naturally aerated sodium sulfate
105 solution (10 g/L) at pH 6.5 (no buffer solution and room temperature). This solution was
106 preferred to NaCl to avoid pitting, which can be sensitive to crystallinity, porosity, and the
107 roughness of the materials. Electrodes were connected to an SP-300 potentiostat equipped
108 with a low current probe (Biologic, France). Open circuit potential (OCP) was first recorded
109 for 3 hours to ensure the potential stability and the passive film steady state.

110 Electrochemical impedance spectroscopy measurements were then performed at the OCP
111 with a frequency range of 100 kHz to 10 MHz with 9 points per decade and signal amplitude
112 of 5 Vrms. The electrochemical characterizations were completed by linear sweep
113 voltammetry. A reduction step was performed from the OCP to -0.7 V_{MSE}, and then the
114 potential was reversed to -0.3 V_{MSE}. The scan rate was fixed to 1 mV/s. Only the

potentiodynamic curves from -0.7 V_{MSE} to -0.3 V_{MSE} are shown here since the forward and backward cathodic currents overlap.

2.4 Characterization techniques

The powder was analyzed by X-ray Diffraction (XRD) apparatus from 30 to 80 ° in 2θ/θ mode with a step of 0.5° /min using Cu-Kα radiation at 40 kV and 40mA. The granulometry analysis was performed in dry by laser diffraction using a Malvern equipment (LMS-3000). The morphology of the particles was analyzed by SEM (Hitachi SU-70) coupled with an EDS probe (SDD Apollo XL). Differential scanning calorimetry (DSC) analysis was performed in a Rigaku apparatus at a heating rate of 10 °C/ min from 300 to 700 °C. After corrosion tests at the OCP, a surface analysis was conducted by XPS analysis (Quantum 2000 apparatus (ULVAC-PHI, Inc). A 100 μm spot monochromatic Al Kα source (1486.7 eV) in constant-analyzer-energy mode (pass energy 187.85 eV for wide scan and 58.7eV for regions) was selected to record the spectrum of Fe2p, Cr2p, and Mo3d. Details of the analysis are given later.

3. Results and discussion

3.1 Metallic glass powder, obtaining and Sintering.

The powder obtained by induction oven and gas atomization (Figure 1a) has mainly spherical morphology particles mixed with elongated particles typical of this processing method, as shown in figure 1a. After a sieving process, the particle size showed a lognormal distribution with an average particle size (Dv_{50}) of 24 μm (Figure 1b). Particle size has been shown to affect the densification process during spark plasma sintering. Smaller particle sizes increase

the contact areas and have stronger driving forces increasing the mass migration, which benefits the densification [21,22]. The mean particle size used in this work is similar to the smaller reported for other authors with the same composition [23,24]. Even if sieving was performed, the particle distribution was relatively wide, as confirmed by a SPAM of 1.5. The X-ray diffractogram (Figure 1c) on the powder shows a significant and broad peak, characteristic of the amorphous structures [25].

The DSC test (Figure 1d) shows a glass transition temperature (T_g) of 577 °C and two exothermic peaks, which correspond to two crystalline temperatures T_{x1} and $T_{x2,}$ at 653 and 670 °C, respectively, and a supercooled liquid region ($\Delta T=T_x-T_g$) of 76 °C. T. Paul et al. [26] studied the sintering mass mechanism of a similar amorphous alloy powder by SPS. They found the densification´s onset, which is around 320 °C. The maximum densification rate attended was at ~ 585 °C retaining its amorphous structure. Additionally, they corroborate that the dominant mass transport mechanism during sintering is by viscous flow. On the other hand, A. Shing et al. [27] sintered the same alloy at a temperature close to the Tg (570 °C). They found that it leads to a notable atomic reordering and the formation of medium-range-ordering (MRO) clusters. However, this formation of nanocrystals could reduce the propagation of the shear bands during deformation, increasing the material's hardness. S.P. Harimkar et al. [24] also reported crystallization during SPS at temperatures below the Tx and close to the T_g. Therefore, to avoid devitrification, temperatures below the Tg were used for this work.

Figure 2 shows the sintering cycles applied to the metallic glass powder to produce BMG samples. The cycles S1 and S2 almost overlap even if they do not exactly follow the same

steps. For S1, the maximum temperature (575 °C) was reached in one step with a 50 °C/min heating rate. Because of the SPS's temperature control system (PID), the maximum temperature was overtaken for a short period (~2 min). To avoid it, the cycle S2 was designed to reach (i) 560 °C with a heating rate of 50 °C/min and then (ii) 575 °C with a heating rate of 1 °C/min. For the cycle S3, the powder was heated up to 555 °C with a rate of 50 °C. Then, the temperature of 575 °C was reached with a 1 °C/min heating rate. With this procedure, the cycle S3 took 15 min more than S1 and S2. Note that the materials' sintering time has an important role since it can induce crystallization or crystal growth [24,28]. The samples obtained after SPS had a diameter of ~14 mm and a thickness of ~10 mm. They were labeled as S1, S2, and S3, depending on the sintering cycled used.

XRD patterns on S1, S2, and S3 samples are reported in figure 3a. The diffractograms show the coexistence of amorphous and crystalline structures with a ratio that depends on the SPS cycle. Thus, S1 presents the highest degree of crystallization, while S3 remains mostly amorphous. According to figure 3a, S2 presents an intermediate behavior. For S1, two kinds of carbides precipitates were identified: $(Fe, Cr)_{23}$ $(B, C)_6$ (ICDD 98-061-2585) and $C_1Cr_2Fe_{14}$ (ICDD 98-007-6800). The S2 diffractogram shows similar peaks as S1 characteristics of carbides but with lower intensity, suggesting a higher ratio of the amorphous phase. After cycle S3, the sample remains mostly amorphous with low-intensity peaks characteristics of chromium iron carbide $C_1Cr_2Fe_{14}$. The samples' crystallinity percentage was calculated with the formula proposed by M. Ohlberg et al. [29] for partially devitrified glasses using the X-ray diffractograms. The crystallinity obtained in the samples is 70 %, 24 %, and 19 % for S1, S2, and S3, respectively, with a standard deviation of ±5 %.

https://doi.org/10.1016/j.jallcom.2021.160399.

The samples' density (Figure 3b) showed the highest value for sample S2 with 87 %, followed by the S1 sample with 85 % and S3 with 83 %. Even though the final temperature was the same for the three cycles, the sintering heating rate affects the material's activation energy. The sintering time of sample S3 is longer than the other samples, due to the very slow heating rate, but the crystallinity percentage of the sample is the lowest as well as the density (Figure 3). This phenomenon was also observed by L. H. Liu et al. [30]; they found out that the behavior of viscous flows is different during SPS sintering; slow rates of heating increase the activation energy for mass transportation as it is demonstrated with a lower density in sample S3. Tanaji Paul et al. [31] predicted the viscous flow activation energy dependence on the heating rate by the Arrhenius equation and the directional structural relaxation model, demonstrating a viscosity dependence on the heating rate at temperatures lower than the Tg. They modeled different heating rates and demonstrated that the activation energy decreases with the heating rate's increments.

Additionally, to this effect, it should be considered the effective time at the final temperature. Sample S1 had a holding time of 15 min at the maximum temperature, which can induce devitrification, and with it, an increase in the viscosity affecting the densification process. Tanaji Paul et al. [32] studied the effect of SPS annealing on a BMG Fe-based alloy's crystallization behavior with a similar composition to the one used in this work. They established that during the annealing time, the pre-existing nuclei grow into well-developed crystals, and the increase in the duration of isothermal annealing causes an increase in the volume fraction of all crystal sizes in the material. It implies that during the sintering cycle S1, crystals were formed during the heating process and grew during the holding time.

https://doi.org/10.1016/j.jallcom.2021.160399.

Figure 4 shows the SEM top surface images of the edges, the centers, and the cross-section of samples S1, S2, and S3. The micrographs of the edge top surface (Figure 4a) show that the particles are in an initial sintering stage where their morphology is almost as in the initial state suggesting local bonding mechanisms in the outer region. This area still is very porous. In the center of the sample (Figure 4b), metallic glass particles merge more or less well as a cycle function. The morphology of the particles is no longer observed in samples S1 and S2. However, in sample S3 their morphology is still distinguishable. However, they have already formed and grown necks during the sintering process. S3 sample have an evident porosity, which is not observed in S1 and S2 samples. Finally, in the cross-section micrographs (Figure 4c), it can be observed how the densification changes in each sample. In S1 sample it can be observed different degrees of sintering. It has areas where the particles are totally cohered and others where they just have necks formation. In the S2 sample, it is observed higher densification on the top than in the center. The particles in the top are cohered with some remaining porosity while in the center of the sample, still possible to observe the particles' morphology, and the sample is very porous. S3 sample shows a more homogeneous sintering degree between the top and the center, but it is more porous than samples S1 and S2.

The difference of densification between the edge and the center observed for all the samples in the micrographs (the centers are higher densified than the edges) and a difference in density from the top to the center is a direct consequence of the establishment of two gradients of temperature in the SPS mold. The first gradient is axial from the bottom to the top surface of the sample. The second gradient is radial from the center to the edge of the sample. Note that the gradient amplitude is modified by the diameter and thickness of the sample produced. According to Tanaji et al. [33], for a similar composition of metallic glass as this work, the

radial temperature gradient during SPS for a die of 15 mm is ~29 °C between the center and the die wall (where the thermocouple is located) when a heating rate of 100 °C/min is applied. The ΔT is directly proportional to the heating rate; for a heating rate of 50 °C/min, the temperature gradient is ~14.5 °C.

On the one hand, S1 presents the highest degree of cohesion between the grain, a relative density of 85 %, and a crystallinity ratio of 70 %. On the other hand, SEM images on S3 show particles not entirely interconnected in the center of the sample, consistent with the low relative density (about 83 %) and a low degree of crystallinity (19 %). The sample S2 presents a compromise between the densification, the particle's cohesion, and the crystallinity degree.

Even if S2 presents an average behavior, further material optimization was performed from the sintering cycle S3. Indeed, the crucial point is to keep the amorphous structures of the alloys.

3.2 Optimization of BMG materials

In SPS, the applied pressure during the process aids in particle arrangement. It enhances the sintering kinetics, while the temperature enhances the atomic motion, and with it, the diffusion process, but in metallic glasses, also promotes crystallization. Note that the temperature should be above 535 °C of a Fe-alloy to activate particle deformation playing a role in the material densification [34]. Therefore, the final temperature was decreased at 560 ℃ to avoid crystallization, but the axial pressure of samples S4 was increased from 50 MPa to 100, 200, 300, and 400 MPa. Additionally, to reduce the axial thermal gradient, the powder used was decreased from 7 g to 3.5 g.

https://doi.org/10.1016/j.jallcom.2021.160399.

X-ray diffractograms were recorded on the new samples with the conditions mentioned above. Figure 5a reports the X-ray pattern for each pressure. It is worth noticing that the crystalline phase observed previously at 575 °C and 50 MPa is no longer detected, with a maximum temperature of 560 °C. Therefore, a reduction of 10 °C of Tf is beneficial to keep the material's amorphous state. Whatever the pressure, only amorphous peaks are observed on diffractograms confirming that the higher sintering pressure does not affect the volume fraction of the amorphous phase until the temperature is carefully selected. Note that this trend may be alloy-dependent, as Maurya et al. [35] observed with the consolidation pressure of amorphous Al alloys by SPS.

Relative densities of the samples are reported as a function of the pressure in figure 5b. A linear increase in density is observed from 50 to 200 MPa. Above this pressure, the density stabilizes about 98 %. The improvement of the density with the pressure was already theoretically analyzed by Paul et al. [34] on Fe-based amorphous alloys. They stated that the compressive viscous flow deformation of the particles was pressure dependent. The increase in density is then obtained through plastic deformation, and the sliding of the grain boundaries occurs to a larger extent at higher pressures. The high density also results in the particle size distribution and the presence of small elements that easily fill the voids and reduce porosities [36]. In figure 6, SEM images of the Fe-alloy BMG samples at different uniaxial pressures are shown. In the images, we can observe the effect of the pressure on the densification in the specimens at 50 and 100 MPa; the particles are slightly interconnected, the morphology of the particles does not yet present a change. At these parameters, the sintering process is in an early stage. The micrography of the sample at 200 MPa, shows a high increment in densification compared with the two previous samples; at this pressure, the

particles emerged just with a remaining porosity between them. This also confirms the results obtained for the relative density (Figure 5b). The samples at 300 and 400 MPa showed an increase in densification with just a few remnant porosities on the surface. However, the 300 MPa sample has a denser surface, which is in coherence with the relative density results. The S4-300 sample's cross-section showed defects in the specimen due to particle's detachment during the cutting and polishing process and maybe due to a low cohesive force between them. The cross-section of the sample also shows a homogeneous density through the sample.

The 15 °C reduction in the final temperature resulted beneficial in preserving the material's amorphous phase but significantly affected the sintering process. With the same sintering cycle and pressure as sample S3, sample S4-50 decreased in density from 83 % to 69 %. The increase in applied pressure proved to be effective in mitigating this effect and enabling to obtain higher densities.

3.3. OCP behavior and passive film composition

Electrochemical tests were performed to evaluate the crystallinity and the relative density influence on the Fe-Cr BMG´s corrosion resistance. These tests were performed on S1, S2, and S3 samples and compared with S4-300, in which any crystallization was observed by XRD and had the highest relative density and homogeneity of the produced samples. Note that reproducibility tests were carried out, and the results overlap well. Therefore, only the trend curves are reported below.

https://doi.org/10.1016/j.jallcom.2021.160399.

It must be noticed that the presence of a gradient density may affect the electrochemical response of the systems. Assuming no variation in the chemical composition along the sample diameter, the electrochemical reactivity of the surface should be affected by the roughness induced by the open pores at the surface; rough passive surfaces are more sensitive to localized corrosion than flat ones [37]. This phenomenon is increased if pores are interconnected. In the following, macroscopic electrochemical tests were performed, knowing that they may underestimate surface reactivity since a macroscopic behavior is recorded [38]. To further in the effect of edge-center porosity of samples, local electrochemical analysis should be applied, which does not fall under this paper's scope [39].

Figure 7a shows the Open Circuit Potential recorded on SPS samples in the aerated sulfate solution (neutral pH, room temperature, and stagnant condition). Whatever the sample, the steady-state potential is reached after 1×10^6 seconds of immersion. S1 presents the most anodic value at about -0.4 VMSE, followed by S2 and S3 at about -0.45 VMSE. Note that the difference of 50 mV might not be significant since a slight deviation of the potential is still detected for S2 and S3. In Figure 7a, S4-300 present the most active potential at about -0.52 VMSE. For this sample, the dropout of potential was confirmed on reproducibility tests and always occurred below 6×10^4 seconds. Note that this potential transient is not understood yet.

Yang et al. [40] already reported such a trend focusing on the content of Mo, Cr, and Iron at the oxide state. For experimental confirmation, XPS analyses were performed on SPS samples after immersion at the OCP. Fe2p, Cr2p, and Mo3d were recorded. XPS peak software was used to fit the XPS spectra (Figure 8). Based on the literature [41,42] and open

database *La surface.com*, Fe2p was split into two regions: 706-707 eV and 708-714 eV. The first region was assigned to Fe° metallic state, and the second region was attributed to Fe oxidic states. The Cr 2p peak consisted of three peaks at around 573-571 eV, 575-576 eV, and 577-578 eV for the metallic state, Cr3+, and Cr6+ oxidic states, respectively. For the Mo 3d spectra, six peaks were used. Two peaks between 227-228 eV and 230-231 eV corresponded to Mo° metallic state. Two other peaks at 228-229 eV and 233-234 eV were assigned to Mo^{4+} oxidic state. Finally, the peaks between 231-232 eV and 234-236 eV were attributed to Mo^{6+} oxidic state. Figure 8 illustrates the XPS fit results of the Fe 2p, Cr 2p, and Mo 3d peaks for S1 (70% of crystallinity) and S4 (1% of crystallinity). The atomic concentration of these metallic elements was calculated from the metallic and oxidic state areas, for Yang et al.[40], the amorphous state of the material facts on the quantity of Cr- and Mo- oxides in the passive. Therefore, the quantity β was calculated from equation 1. Results of Equation 1 are reported in Table 2. They show an increase in the quantity of Cr- and Mo-oxide species on the surface with the crystallinity reduction of the samples. Consequently, the differences in passive currents on polarization curves and EIS experiments could be expected.

$$\beta = \frac{A_{Cr\ 2p} + A_{Mo\ 3d}}{A_{Cr\ 2p} + A_{Mo\ 3d} + A_{Fe\ 2p}} \qquad \text{Equation 1.}$$

With the large concentration of carbon in the material, the formation of MxCy carbides and intermetallic compounds were detected by X-ray diffraction (Figure 3). Depending on the thermal treatment, the carbide concentration reduces from S1 to S4. Precipitation of carbides is known to create a depletion area in Fe, Cr around. These places are then less covered by a stable and chrome-enriched film and are easily attacked.

https://doi.org/10.1016/j.jallcom.2021.160399.

The oxidation state of Mo, Cr, and Fe suggests forming a complex oxide film with a chemistry that may depend on the degree of crystallinity and the Cr/Mo ratio [40,43]. This later information was not confirmed by our XPS analysis either because of the sample's roughness that affects the peak morphology or the immersion duration.

3.5. Surface reactivity in sulfate solution

Figure 7b reports the typical linear sweep voltammetry curves after 3 hours at the OCP. Tafel's fit was performed on polarization curves for maker positions at a minimum of 80 mV of the corrosion potential. EC-Lab software was used to calculate the corrosion potential (E_{corr}), the current density (J_{corr}) at E_{corr}, the Tafel constants (β and βc), and the corrosion rate (Table 2).

The corrosion potential, E_{corr}, follows the trend observed on OCP. The highest cathodic potential is attributed to S4-300, which is the optimized materials in terms of amorphous phase and density. On the opposite, S1 presents the most anodic potential. For Yang et al. [40], the crystallization of Fe-Cr metallic glass alloy results in stabilizing iron oxides instead of chromium or molybdenum oxides. As the surface chemistry change, modifications of the cathodic and anodic behavior are expected.

The cathodic reaction is under a mix charge transfer and mass transport limitation on Tafel's plots, as expected in a neutral, aerated, and stagnant solution. In table 2, the Tafel constants βc are in the range of 120 to 90 mV/decade, corresponding to the hydrogen evolution reaction [44]. Also, one can notice a decrease of βc with sample amorphization. This evolution is

either due to hydrogen reduction or oxide film reduction [40,45]. For the former, crystallinity could play a role in the surface energy linked to the oxide layer's chemical composition and contribute to hydrogen reduction. For the latter, oxide reduction may occur during the cathodic polarization. Depending on the film chemistry, iron oxides may preferentially reduce compare to chromium or molybdenum oxides [46–48]. As the ratio of iron oxide/hydroxides is higher for S1 than S2-S3 and S4-300, the cathodic current is stronger. Consequently, E_{corr} shifts to anodic values.

A passive plateau is observed in the anodic domain for the samples except for S1 (current density at about 500 $\mu A/cm^2$). The passivation domain or pseudo passivation is in the range of the corrosion potential and -0.35 V_{MSE}. This behavior is in agreement with the literature, which reports that partial crystallization of an amorphous structure is detrimental for the nucleation and growth of a passive film as well as its protectiveness even if the passive film chemistry do not differ for the same material at the crystalline or amorphous state [41]. Above -0.35 V_{MSE}, the transpassive region starts with the selective dissolution of iron and chromium, as observed on stainless steel passive film [49]. The oxide nature also accounts for corrosion resistance. Less anodic current is required to maintain the steady-state passive film on amorphous materials than on semi-crystalline ones (Figure 7b and values of β_a in table 2). Consequently, the corrosion rate can be mitigated when fully amorphous materials are produced.

After 3 hours of immersion, electrochemical impedance spectra (EIS) were recorded at the OCP. In figure 9, Nyquist diagrams are characterized by a pseudo-capacitive loop online with a passive film's growth in a sulfate solution. On the one hand, the semi-circle loop increases

with the amorphous state of the bulk material, evidencing the beneficial effect of amorphous surfaces for corrosion resistance as reported for other chemical composition [15,50]. On the other hand, S1 is characterized by a constant phase of 45° for low frequencies values associated with reactions limited by diffusion processes [51].

EIS diagrams were fitted using the two electrical equivalent circuits (EEC) reported in table 2. Both EEC are made with a constant phase element (CPE), Q_{dl}, related to the space charge and double-layer capacitance of the passive layer parallel to a resistance, R_{ct}, which expresses the charge transfer resistance associated with the faradic processes of oxidation and reduction (Equation 2). The CPE was preferred to the ideal capacitor (C_{dl}) because of the sample surface heterogeneities and roughness. Using Brugg's approximation, it is possible to estimate the space charge capacitance C_{sc} with Equation 3. For S1, the diffusion process at low frequency is modeled by a Warburg semi-infinite diffusion element where σ_1 is the Warburg coefficient (Eq .4). Note that W is added in serial with R_{ct}. For both EEC, Re represents the electrolyte resistance.

$$Z(f)_{CPE} = [Q_{dl}.(2\pi f)^{n}\ ]^{-1} \qquad \text{Equation 2}$$

$$\frac{1}{2\pi(R_t.Q_{dl})^{1/n}} = \frac{1}{2\pi R.C_{dl}} \qquad \text{Equation 3}$$

$$Z(f)_W = \frac{\sqrt{2}.\sigma_1}{\sqrt{j.2.\pi f}} \qquad \text{Equation 4}$$

Table 2 lists the EEC fit results, whereas the lines plotted in figure 9 show the fit results. R_e is in the range of 50 to 150 Ohm cm² for all the tests, which is expected for a sulfate solution at 10 g/L. The crystallinity state induces a polarization resistance increase confirming the underneath microstructure's role in the passive film grown [51–54].

https://doi.org/10.1016/j.jallcom.2021.160399.

For Q_{dl} and n, the results in table 2 show a significant difference between crystalline (i.e., S1) and quasi amorphous structures (i.e., S2, S3, and S4-300). Q_{dl} is about a few hundred $Fs^{(n-1)}$ cm^{-2} for crystalline samples and drops to a few ten $Fs^{(n-1)}$ cm^{-2} for the degree of crystallinity lower than 30 %. Note that C_{dl} follows the same trend. On the one hand, the parameter *n* is about 0.6, which is characteristic of limited reactions through nano-micro porous structures [55–57]. The transmission line model and its derivatives were proposed to consider the pore size geometry, distribution on the impedance in the absence of diffusion [58,59]. Some works also proposed quantifying the porosity properties (number, length, radius) from the impedance data [57,60,61]. These approaches fall under this work scope as this behavior was only found for the most crystalline sample.

On the other hand, the parameter n is at approximately 0.8 for the three other samples. The deviation from the ideal capacitor (n=1) is attributed to the metallurgical defects (voids, vacancies) in the space charge volume and the surface morphology, which is not smooth since samples were only polished to SiC 4000. Morphological gradients also exist from the center to the samples' outer region (Figure 4) [48,62,63]. Therefore, the bulks' crystallization and its consequences on the passive film structure are detrimental to its intrinsic resistance and not only regarding its nucleation and growth, as seen before.

Regarding the corrosion properties of the four Fe-based samples, there is a significant effect of SPS parameters on the surface reactivity. Whatever the sintering cycle selected, an oxide layer grows on the alloy surface. If operating conditions are suitable for amorphous structures, the Cr and Mo content in the oxide layer increases instead of Fe. The surface becomes passives and is characterized by a steady-state current in the passive range of a few

419 μA/cm². The passive domain is similar to all samples regardless of the iron content in the
420 film, suggesting that the oxide layer is not only formed by chromium oxide but a dual or
421 duplex oxide mixing Cr, Mo, and Fe. The tuning SPS parameter also has a consequence on
422 the degree of porosity. It must be noticed that porosity increases with the degree of
423 crystallinity.

424 Porosity and, more generally, surface defects are prone to localized corrosion phenomena. In
425 a chloride-free environment, the general dissolution behavior of materials is only
426 characterized. The metallurgical study showed an absence of homogeneity in the porosity
427 distribution along the sample's diameters. Indeed, the SPS process is more efficient on the
428 samples' center than on edge. This gradient of defects also has a consequence on corrosion
429 behavior. As the porosity increases, the corrosion resistance of the material changes. In
430 addition to the chemical composition of the oxide layer, the porosity on the surface (i.e.,
431 roughness) and pore interconnection give suitable conditions for localized corrosion. If the
432 oxide layer is not strong enough (no pure chromium oxide layer), dissolution can start more
433 quickly. Further work should focus on the local electrochemical of SPS samples, comparing
434 edge and center reactivities to go deep in the local effect of crystallinity, porosity on micro
435 galvanic coupling with a denser and amorphous area of the sample.

436 **4. Conclusions**

437 Spark plasma sintering is a technique that facilitates the processing of amorphous alloys. The
438 heating rate plays an important role in the activation energy; for super viscous materials, slow
439 heating rates increase it, which was beneficial to conserve the amorphous phase in this case,
440 but the material's densification was reduced. This effect can be compensated with the

increment of the uniaxial pressure. In the SPS, the slow heating rates also reduce the temperature gradient allowing a homogeneous densification process.

Materials porosity reduces the corrosion resistance of the materials. However, for metallic glasses, more advantages have been found in preserving the material's amorphous phase than reaching higher densities.

Acknowledgments

L. Zarazúa-Villalobos acknowledge CONACYT (Mexican Council of Science and Technology) for the fellowship granted. JSPS KAKENHI Grant Number JP19K05092 supported this work. Masatoshi Tanno (Tohoku University, Niche) is also acknowledged for the XPS analysis.

References

[1] M.D. Demetriou, A. Wiest, D.C. Hofmann, W.L. Johnson, B. Han, N. Wolfson, G. Wang, P.K. Liaw, Amorphous metals for hard-tissue prosthesis, JOM. 62 (2010) 83–91. doi:10.1007/s11837-010-0038-2.

[2] P.C. Wong, P.H. Tsai, T.H. Li, C.K. Cheng, J.S.C. Jang, J.C. Huang, Degradation behavior and mechanical strength of Mg-Zn-Ca bulk metallic glass composites with Ti particles as biodegradable materials, J. Alloys Compd. 699 (2017) 914–920. doi:10.1016/j.jallcom.2017.01.010.

[3] O. Baulin, D. Fabrègue, H. Kato, A. Liens, T. Wada, J.M. Pelletier, A new, toxic element-free Mg-based metallic glass for biomedical applications, J. Non. Cryst. Solids. 481 (2018) 397–402. doi:10.1016/j.jnoncrysol.2017.11.024.

[4] H.F. Li, Y.F. Zheng, Recent advances in bulk metallic glasses for biomedical applications, Acta Biomater. 36 (2016) 1–20. doi:10.1016/j.actbio.2016.03.047.

[5] S. Sharma, C. Suryanarayana, Mechanical crystallization of Fe-based amorphous alloys, J. Appl. Phys. 102 (2007) 083544. doi:10.1063/1.2800840.

[6] K.K. Xu, A.D. Lan, H.J. Yang, P.D. Han, J.W. Qiao, Corrosion behavior and pitting susceptibility of in-situ Ti-based metallic glass matrix composites in 3.5 wt.% NaCl solutions, Appl. Surf. Sci. 423 (2017) 90–99. doi:10.1016/j.apsusc.2017.06.145.

[7] L. Liu, C. Zhang, Fe-based amorphous coatings: Structures and properties, Thin Solid Films. 561 (2014) 70–86. doi:10.1016/j.tsf.2013.08.029.

[8] L. Xie, Y.-M. Wang, X. Xiong, Z.-K. Chen, Comparison of Microstructure and Tribological Properties of Plasma, High Velocity Oxy-Fuel and Detonation Sprayed Coatings from an Iron-Based Powder, Mater. Trans. 59 (2018) 1591–1595. doi:10.2320/matertrans.M2018141.

[9] J. Henao, A. Concustell, I.G. Cano, N. Cinca, S. Dosta, J.M. Guilemany, Influence of Cold Gas Spray process conditions on the microstructure of Fe-based amorphous coatings, J. Alloys Compd. 622 (2015) 995–999. doi:10.1016/j.jallcom.2014.11.037.

[10] A. Singh, S.R. Bakshi, A. Agarwal, S.P. Harimkar, Microstructure and tribological behavior of spark plasma sintered iron-based amorphous coatings, Mater. Sci. Eng. A. 527 (2010) 5000–5007. doi:10.1016/j.msea.2010.04.066.

[11] Z.H. Chu, H. Kato, G.Q. Xie, G.Y. Yuan, W.J. Ding, A. Inoue, Consolidation and mechanical properties of Cu 46Zr 42Al 7Y 5 metallic glass by spark plasma sintering, J. Non. Cryst. Solids. 358 (2012) 1263–1267. doi:10.1016/j.jnoncrysol.2012.02.027.

[12] K.R. Ravi, Indumathi, R. Subramanian, B.S. Murty, Spark Plasma Sintering of Fe-Cr-Mo-P-B-C-Si Amorphous Alloy, Mater. Sci. Forum. 710 (2012) 320–325. doi:10.4028/www.scientific.net/MSF.710.320.

[13] Y. Waseda, K.T. Aust, Corrosion behaviour of metallic glasses, J. Mater. Sci. 16 (1981) 2337–2359. doi:10.1007/BF01113569.

[14] M.J. Duarte, J. Klemm, S.O. Klemm, K.J.J. Mayrhofer, M. Stratmann, S. Borodin, a. H. Romero, M. Madinehei, D. Crespo, J. Serrano, S.S. a. Gerstl, P.P. Choi, D. Raabe, F.U. Renner, Element-Resolved Corrosion, Science (80-.). 372 (2013) 372–377. doi:10.1126/science.1230081.

[15] S.L. Wang, H.X. Li, X.F. Zhang, S. Yi, Effects of Cr contents in Fe-based bulk metallic glasses on the glass forming ability and the corrosion resistance, Mater. Chem. Phys. 113 (2009) 878–883. doi:10.1016/j.matchemphys.2008.08.057.

[16] H.S. Ni, X.H. Liu, X.C. Chang, W.L. Hou, W. Liu, J.Q. Wang, High performance amorphous steel coating prepared by HVOF thermal spraying, J. Alloys Compd. 467 (2009) 163–167. doi:10.1016/j.jallcom.2007.11.133.

[17] S.J. Pang, T. Zhang, K. Asami, A. Inoue, Bulk glassy Fe–Cr–Mo–C–B alloys with high corrosion resistance, Corros. Sci. 44 (2002) 1847–1856. doi:10.1016/S0010-938X(02)00002-1.

[18] Z.M. Wang, Y.T. Ma, J. Zhang, W.L. Hou, X.C. Chang, J.Q. Wang, Influence of yttrium as a minority alloying element on the corrosion behavior in Fe-based bulk metallic glasses,

L. Zarazúa-Villalobos, N. Mary, J. Soo-Hyun, K. Ogawa, H. Kato, Y. Ichikawa, Microstructure and corrosion study of Fe-based bulk metallic glass obtained by spark plasma sintering, Journal of Alloys and Compounds, Volume 880, 2021, 160399, ISSN 0925-8388,

Electrochim. Acta. 54 (2008) 261–269. doi:10.1016/j.electacta.2008.08.017.

[19] T. Paul, S.P. Harimkar, Viscous flow activation energy adaptation by isochronal spark plasma sintering, Scr. Mater. 126 (2017) 37–40. doi:10.1016/j.scriptamat.2016.08.018.

[20] T. Paul, A. Loganathan, A. Agarwal, S.P. Harimkar, Kinetics of isochronal crystallization in a Fe-based amorphous alloy, J. Alloys Compd. 753 (2018) 679–687. doi:10.1016/j.jallcom.2018.04.133.

[21] Y. Cheng, Z. Cui, L. Cheng, D. Gong, W. Wang, Effect of particle size on densification of pure magnesium during spark plasma sintering, Adv. Powder Technol. 28 (2017) 1129–1135. doi:10.1016/j.apt.2017.01.017.

[22] J.H. Shon, I.B. Song, K.S. Cho, Y. il Park, J.K. Hong, N.K. Park, M.H. Oh, Effect of particle size distribution on microstructure and mechanical properties of spark-plasma-sintered titanium from CP-Ti powders, Int. J. Precis. Eng. Manuf. 15 (2014) 643–647. doi:10.1007/s12541-014-0382-1.

[23] A. Singh, S. Katakam, J. Ilavsky, N.B. Dahotre, S.P. Harimkar, Nanocrystallization in spark plasma sintered Fe48Cr15Mo14Y2C15B6bulk amorphous alloy, J. Appl. Phys. 114 (2013). doi:10.1063/1.4817379.

[24] S.P. Harimkar, S.R. Paital, A. Singh, R. Aalund, N.B. Dahotre, Microstructure and properties of spark plasma sintered Fe-Cr-Mo-Y-B-C bulk metallic glass, J. Non. Cryst. Solids. 355 (2009) 2179–2182. doi:10.1016/j.jnoncrysol.2009.07.007.

[25] A.A. Sorour, A.S. Adeniyi, M.A. Hussein, C.P. Kim, N.M. Al-Aqeeli, Densification and microstructure of Fe-Cr-Mo-B-C alloy fabricated by spark plasma sintering, Mater. Sci. Technol. 2018, MS T 2018. (2019) 1454–1461. doi:10.7449/2018/MST_2018_1454_1461.

[26] T. Paul, S.P. Harimkar, Initial stage densification during spark plasma sintering of Fe-based amorphous alloy powder: Analysis of viscous flow, J. Appl. Phys. 120 (2016). doi:10.1063/1.4964330.

[27] A. Singh, T. Paul, S. Katakam, N.B. Dahotre, S.P. Harimkar, In Situ Nanocrystallization-Induced Hardening of Amorphous Alloy Matrix Composites Consolidated by Spark Plasma Sintering, Jom. 68 (2016) 1932–1937. doi:10.1007/s11837-016-1914-1.

[28] O.A. Graeve, M.S. Saterlie, R. Kanakala, S.D. de la Torre, J.C. Farmer, The kinetics of devitrification of amorphous alloys: The time–temperature–crystallinity diagram describing the spark plasma sintering of Fe-based metallic glasses, Scr. Mater. 69 (2013) 143–148. doi:10.1016/j.scriptamat.2013.02.019.

[29] S.M. OHLBERG, D.W. STRICKLER, Determination of Percent Crystallinity of Partly Devitrified Glass by X-Ray Diffraction, J. Am. Ceram. Soc. 45 (1962) 170–171. doi:10.1111/j.1151-2916.1962.tb11114.x.

[30] L.H. Liu, C. Yang, Y.G. Yao, F. Wang, W.W. Zhang, Y. Long, Y.Y. Li, Densification mechanism of Ti-based metallic glass powders during spark plasma sintering process, Intermetallics. 66 (2015) 1–7. doi:10.1016/j.intermet.2015.06.010.

https://doi.org/10.1016/j.jallcom.2021.160399.

L. Zarazúa-Villalobos, N. Mary, J. Soo-Hyun, K. Ogawa, H. Kato, Y. Ichikawa, Microstructure and corrosion study of Fe-based bulk metallic glass obtained by spark plasma sintering, Journal of Alloys and Compounds, Volume 880, 2021, 160399, ISSN 0925-8388,

[31] T. Paul, S.P. Harimkar, Prediction of heating rate controlled viscous flow activation energy during spark plasma sintering of amorphous alloy powders, J. Phys. D. Appl. Phys. 50 (2017). doi:10.1088/1361-6463/aa77e2.

[32] T. Paul, A. Singh, K.C. Littrell, J. Ilavsky, S.P. Harimkar, Crystallization Mechanism in Spark Plasma Sintered Bulk Metallic Glass Analyzed using Small Angle Neutron Scattering, Sci. Rep. 10 (2020) 1–11. doi:10.1038/s41598-020-58748-3.

[33] T. Paul, A. Singh, S.P. Harimkar, Densification and Crystallization in Fe–Based Bulk Amorphous Alloy Spark Plasma Sintered in the Supercooled Liquid Region, Adv. Eng. Mater. 19 (2017) 1–7. doi:10.1002/adem.201700224.

[34] T. Paul, N. Chawake, R.S. Kottada, S.P. Harimkar, Pressure controlled micro-viscous deformation assisted spark plasma sintering of Fe-based bulk amorphous alloy, J. Alloys Compd. 738 (2018) 10–15. doi:10.1016/j.jallcom.2017.12.147.

[35] R.S. Maurya, A. Sahu, T. Laha, Effect of consolidation pressure on phase evolution during sintering of mechanically alloyed Al86Ni8Y6 amorphous powders via spark plasma sintering, Mater. Sci. Eng. A. 649 (2016) 48–56. doi:10.1016/j.msea.2015.09.109.

[36] M. Pellizzari, A. Fedrizzi, M. Zadra, Influence of processing parameters and particle size on the properties of hot work and high speed tool steels by Spark Plasma Sintering, Mater. Des. 32 (2011) 1796–1805. doi:10.1016/j.matdes.2010.12.033.

[37] K. Jaffré, B. Ter-Ovanessian, H. Abe, N. Mary, B. Normand, Y. Watanabe, Effect of Mechanical Surface Treatments on the Surface State and Passive Behavior of 304L Stainless Steel, Metals (Basel). 11 (2021) 135. doi:10.3390/met11010135.

[38] R. Akid, D.. Mills, A comparison between conventional macroscopic and novel microscopic scanning electrochemical methods to evaluate galvanic corrosion, Corros. Sci. 43 (2001) 1203–1216. doi:10.1016/S0010-938X(00)00091-3.

[39] N. Jadhav, V.J. Gelling, Review—The Use of Localized Electrochemical Techniques for Corrosion Studies, J. Electrochem. Soc. 166 (2019) C3461–C3476. doi:10.1149/2.0541911jes.

[40] Y. Yang, C. Zhang, Y. Peng, Y. Yu, L. Liu, Effects of crystallization on the corrosion resistance of Fe-based amorphous coatings, Corros. Sci. 59 (2012) 10–19. doi:10.1016/j.corsci.2012.02.003.

[41] K. Asami, K. Hashimoto, T. Masumoto, S. Shimodaira, ESCA study of the passive film on an extremely corrosion-resistant amorphous iron alloy, Corros. Sci. 16 (1976) 909–914. doi:10.1016/S0010-938X(76)80010-8.

[42] K. Asami, K. Hashimoto, The X-ray photo-electron spectra ofseveral oxides of iron and chromium, Corros. Sci. 17 (1977) 559–570. doi:10.1016/S0010-938X(77)80002-4.

[43] M.A. Ameer, A.M. Fekry, F.E.T. Heakal, Electrochemical behaviour of passive films on molybdenum-containing austenitic stainless steels in aqueous solutions, Electrochim. Acta. 50 (2004) 43–49. doi:10.1016/j.electacta.2004.07.011.

https://doi.org/10.1016/j.jallcom.2021.160399.

[44] B.E. Conway, B. V. Tilak, Interfacial processes involving electrocatalytic evolution and oxidation of H2, and the role of chemisorbed H, Electrochim. Acta. 47 (2002) 3571–3594. doi:10.1016/S0013-4686(02)00329-8.

[45] A.A. Hermas, M.S. Morad, K. Ogura, A correlation between phosphorous impurity in stainless steel and a second anodic current maximum in H2SO4, Corros. Sci. 41 (1999) 2251–2266. doi:10.1016/S0010-938X(99)00046-3.

[46] L.J. Oblonsky, T.M. Devine, A surface enhanced Raman spectroscopic study of the passive films formed in borate buffer on iron, nickel, chromium and stainless steel, Corros. Sci. 37 (1995) 17–41. doi:10.1016/0010-938X(94)00102-C.

[47] P. Schmuki, In Situ X-Ray Absorption Near-Edge Spectroscopic Study of the Cathodic Reduction of Artificial Iron Oxide Passive Films, J. Electrochem. Soc. 143 (1996) 574. doi:10.1149/1.1836483.

[48] C. Boissy, B. Ter-Ovanessian, N. Mary, B. Normand, Correlation between predictive and descriptive models to characterize the passive film - Study of pure chromium by electrochemical impedance spectroscopy, Electrochim. Acta. 174 (2015) 430–437. doi:10.1016/j.electacta.2015.05.179.

[49] S. Tanaka, N. Hara, K. Sugimoto, Corrosion characteristics of Fe203-Cr203 artificial passivation films under potentiostatic control, Mater. Sci. Eng. A. 98 (1995) 63–69. doi:0921-5093(94)04508-9.

[50] J.R. Scully, A. Gebert, J.H. Payer, Corrosion and related mechanical properties of bulk metallic glasses, J. Mater. Res. 22 (2007) 302–313. doi:10.1557/jmr.2007.0051.

[51] M. Apreutesei, C. Boissy, N. Mary, M. Arab Pour Yazdi, A. Billard, P. Steyer, Binary Zr-Ni/Co metallic glass films: Role of the structural state on their durability, Acta Mater. 89 (2015) 305–314. doi:10.1016/j.actamat.2015.01.056.

[52] S. Liu, L. Huang, S. Pang, Effect of microstructure on corrosion behaviours of a Ni-based metallic glass, Rare Met. 30 (2011) 529–532. doi:10.1007/s12598-011-0339-9.

[53] C.A. Gervasi, C.M. Méndez, P.D. Bilmes, C.L. Llorente, Analysis of the impact of alloy microstructural properties on passive films formed on low-C 13CrNiMo martensitic stainless steels, Mater. Chem. Phys. 126 (2011) 178–182. doi:10.1016/j.matchemphys.2010.11.043.

[54] C.-O.. Olsson, D. Landolt, Passive films on stainless steels—chemistry, structure and growth, Electrochim. Acta. 48 (2003) 1093–1104. doi:10.1016/S0013-4686(02)00841-1.

[55] M. Mokhtari, T. Wada, C. Le Bourlot, J. Duchet-Rumeau, H. Kato, E. Maire, N. Mary, Corrosion resistance of porous ferritic stainless steel produced by liquid metal dealloying of Incoloy 800, Corros. Sci. 166 (2020) 108468. doi:10.1016/j.corsci.2020.108468.

[56] S.J. Cooper, A. Bertei, D.P. Finegan, N.P. Brandon, Simulated impedance of diffusion in porous media, Electrochim. Acta. 251 (2017) 681–689. doi:10.1016/j.electacta.2017.07.152.

[57] O.E. Barcia, E. D'Elia, I. Frateur, O.R. Mattos, N. Pébère, B. Tribollet, Application of the

615 impedance model of de Levie for the characterization of porous electrodes, in: Electrochim.
616 Acta, 2002: pp. 2109–2116. doi:10.1016/S0013-4686(02)00081-6.

617 [58] X.Y. Wang, J. Yan, H.T. Yuan, Y.S. Zhang, D.Y. Song, Impedance studies of nickel hydroxide
618 microencapsulated by cobalt, Int. J. Hydrogen Energy. 24 (1999) 973–980.
619 doi:10.1016/S0360-3199(98)00130-X.

620 [59] H. Keiser, K.D. Beccu, M.A. Gutjahr, Abschätzung der porenstruktur poröser elektroden aus
621 impedanzmessungen, Electrochim. Acta. 21 (1976) 539–543. doi:10.1016/0013-
622 4686(76)85147-X.

623 [60] C. Hitz, A. Lasia, Experimental study and modeling of impedance of the her on porous Ni
624 electrodes, J. Electroanal. Chem. 500 (2001) 213–222. doi:10.1016/S0022-0728(00)00317-X.

625 [61] O.E. Barcia, S. Cattarin, E. D'Elia, I. Frateur, O.R. Mattos, M. Musiani, N. Pébère, B. Tribollet,
626 Further to the paper "application of the impedance model of de Levie for the
627 characterization of porous electrodes" by Barcia et al. [Electrochim. Acta 47 (2002) 2109],
628 Electrochim. Acta. 51 (2006) 2096–2097. doi:10.1016/j.electacta.2005.06.035.

629 [62] S. Marcelin, B. Ter-Ovanessian, B. Normand, Electronic properties of passive films from the
630 multi-frequency Mott-Schottky and power-law coupled approach, Electrochem. Commun.
631 66 (2016) 62–65. doi:10.1016/j.elecom.2016.03.003.

632 [63] P. Córdoba-Torres, T.J. Mesquita, R.P. Nogueira, Relationship between the origin of constant-
633 phase element behavior in electrochemical impedance spectroscopy and electrode surface
634 structure, J. Phys. Chem. C. 119 (2015) 4136–4147. doi:10.1021/jp512063f.

635

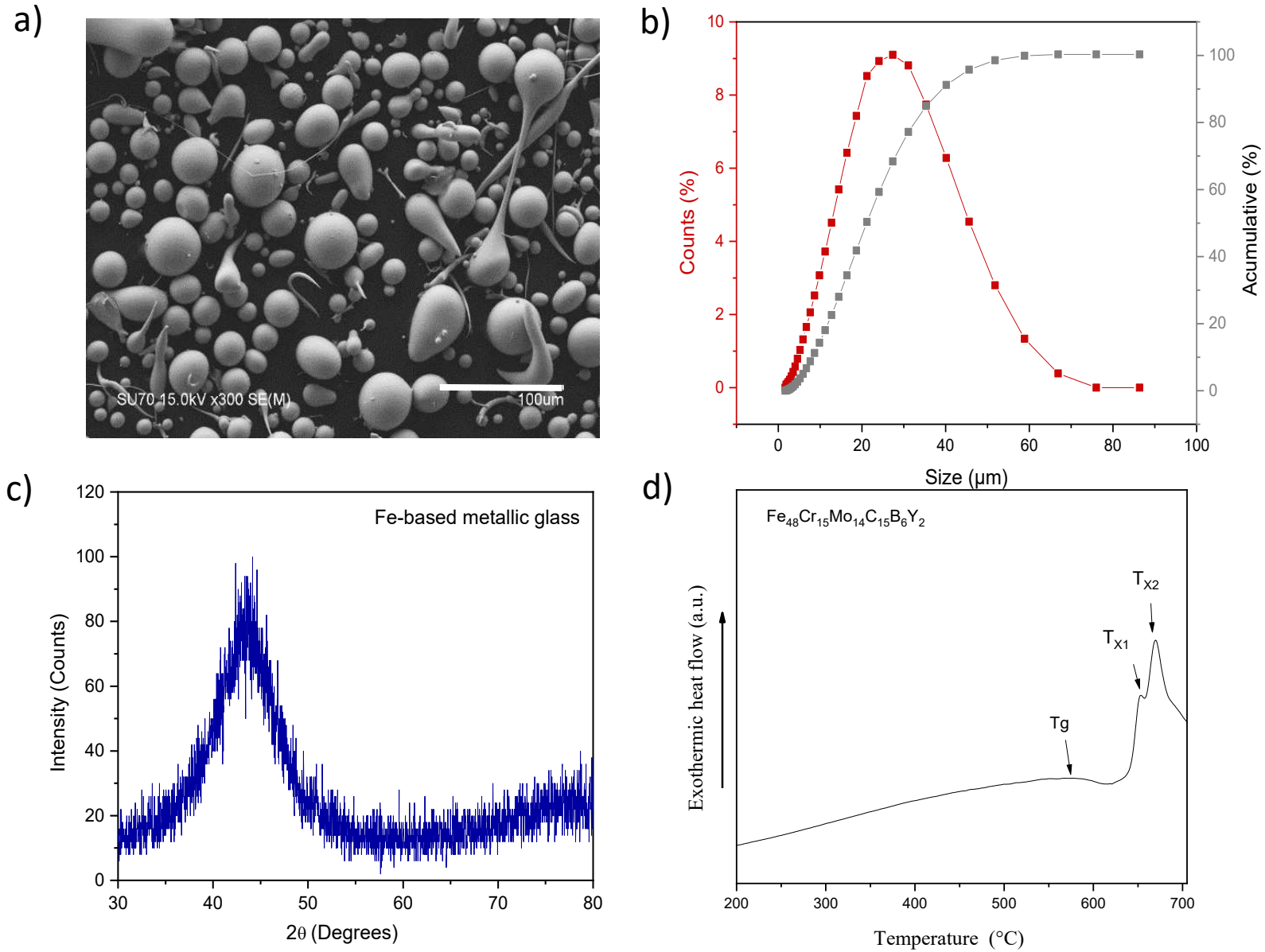

Figure 1. Powder of Fe-base metallic glass, a) SEM observations, b) Size distribution by laser granulometry, c) XR-Diffraction and d) DSC.

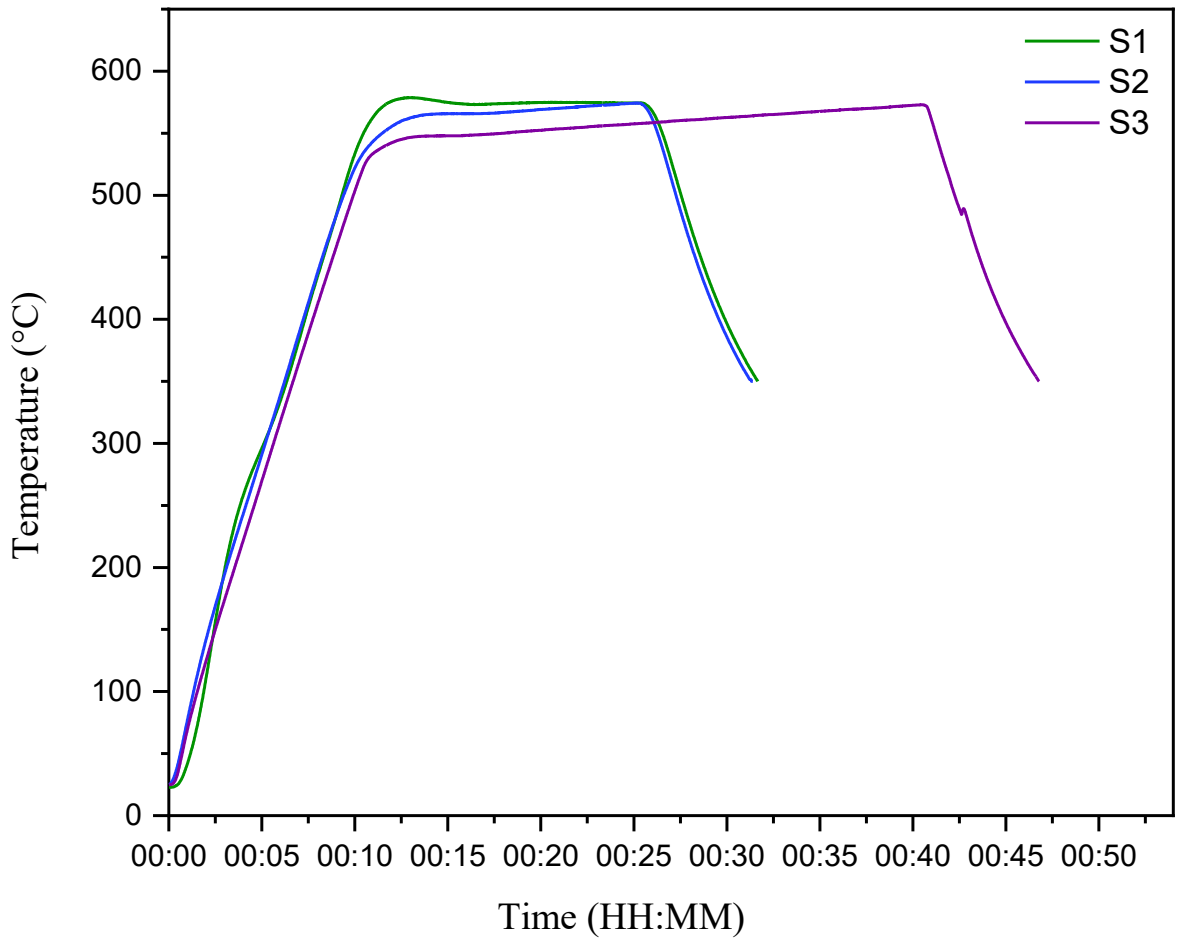

Figure 2.Sintering cycles S1, S2 and S3 with final temperature of 575 ℃. Axial pressure 50 MPa.

Sample name	Maximum temperature	Maximum Pressure
S1 – S2 – S3	575 °C	50 MPa
** Differences are in the sintering cycle:*		
S1 = Room temperature to 575 ℃ at 50 ℃/min and 15 min of holding time		
S2 = Room temperature to 560 ℃ at 50 ℃/min then to 575 ℃ at 1 ℃/min		
S3 = Room temperature to 545 ℃ at 50 ℃/min then to 575 ℃ at 1 ℃/min		
S4-50	560 °C	50 MPa
S4-100	560 °C	100 MPa
S4-200	560 °C	200 MPa
S4-300	560 °C	300 MPa
S4-400	560 °C	400 MPa
** Identical sintering cycle:*		
S4 = Room temperature to 560 ℃ at 50 ℃/min then to 560 ℃ at 1 ℃/min		

Table 1. List of samples and SPS pressure and temperature.

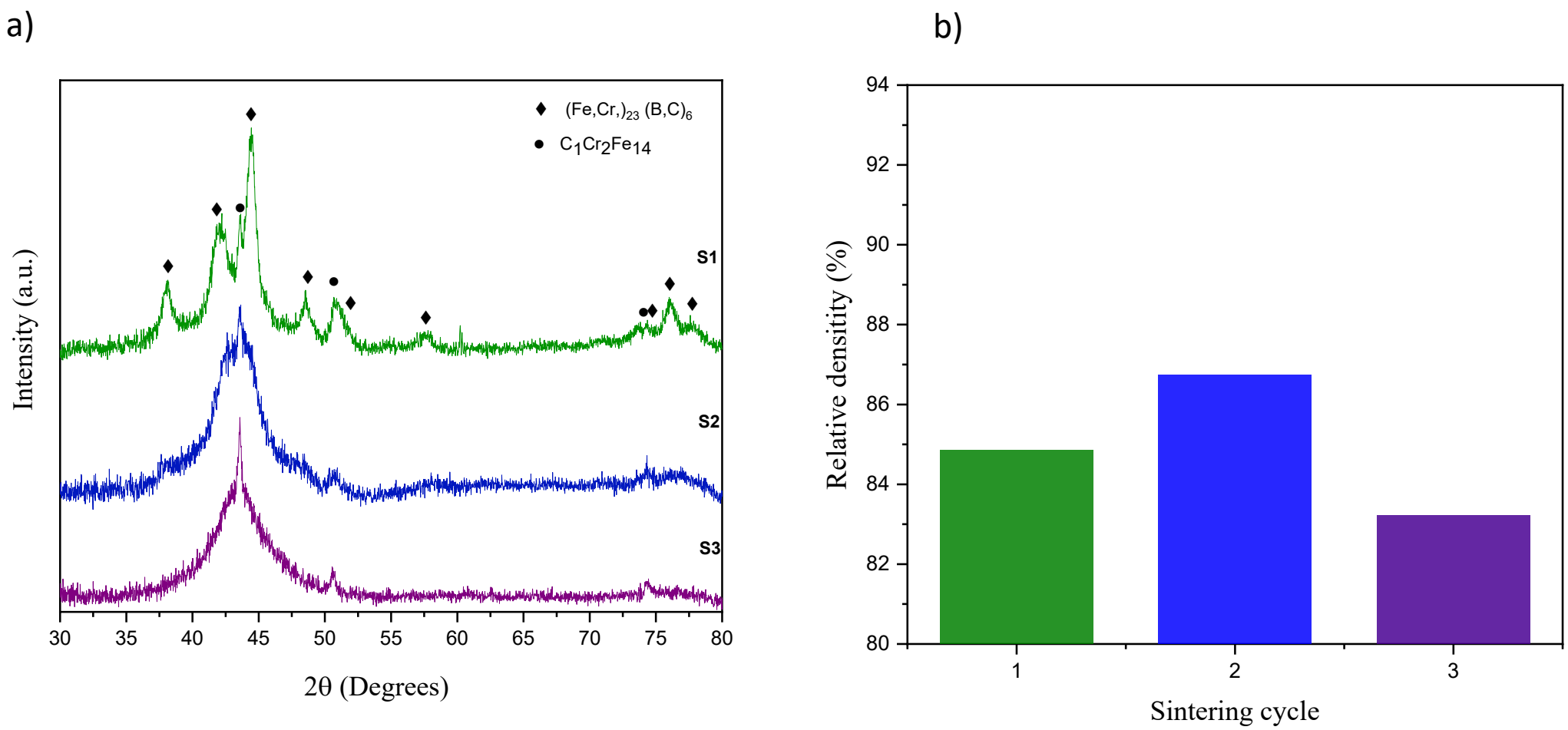

Figure 3. a) X-ray diffraction patterns on BMG and b) density of Fe-base metal glass sintered by S1, S2 and S3 cycles at a maximum temperature of 575 ℃ (axial pressure 50 MPa).

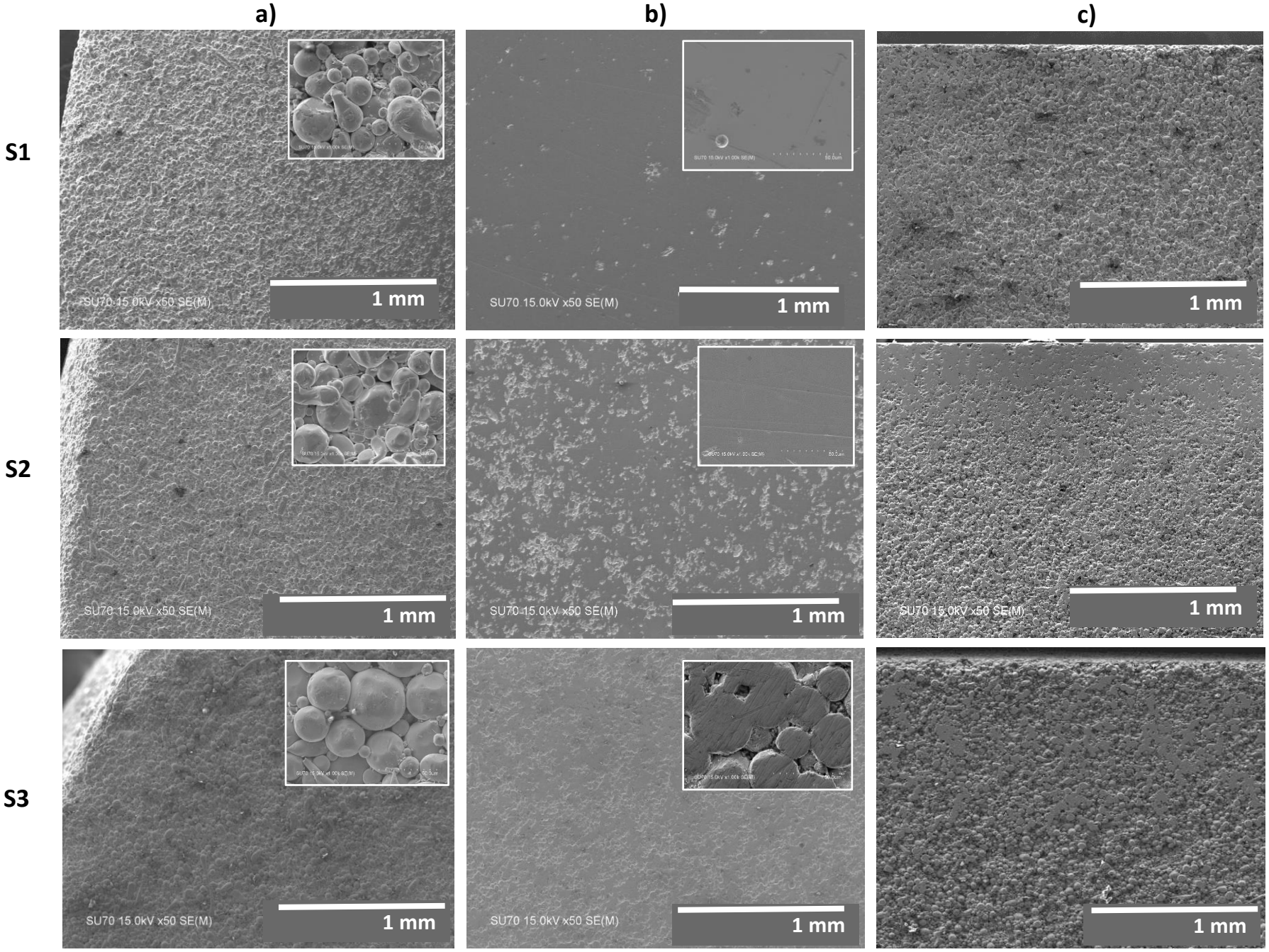

Figure 4. Top surface SEM images of sintered samples (axial pressure 50 MPa) S1, S2, and S3 a) at the edge, b) at the center and c) in cross-section.

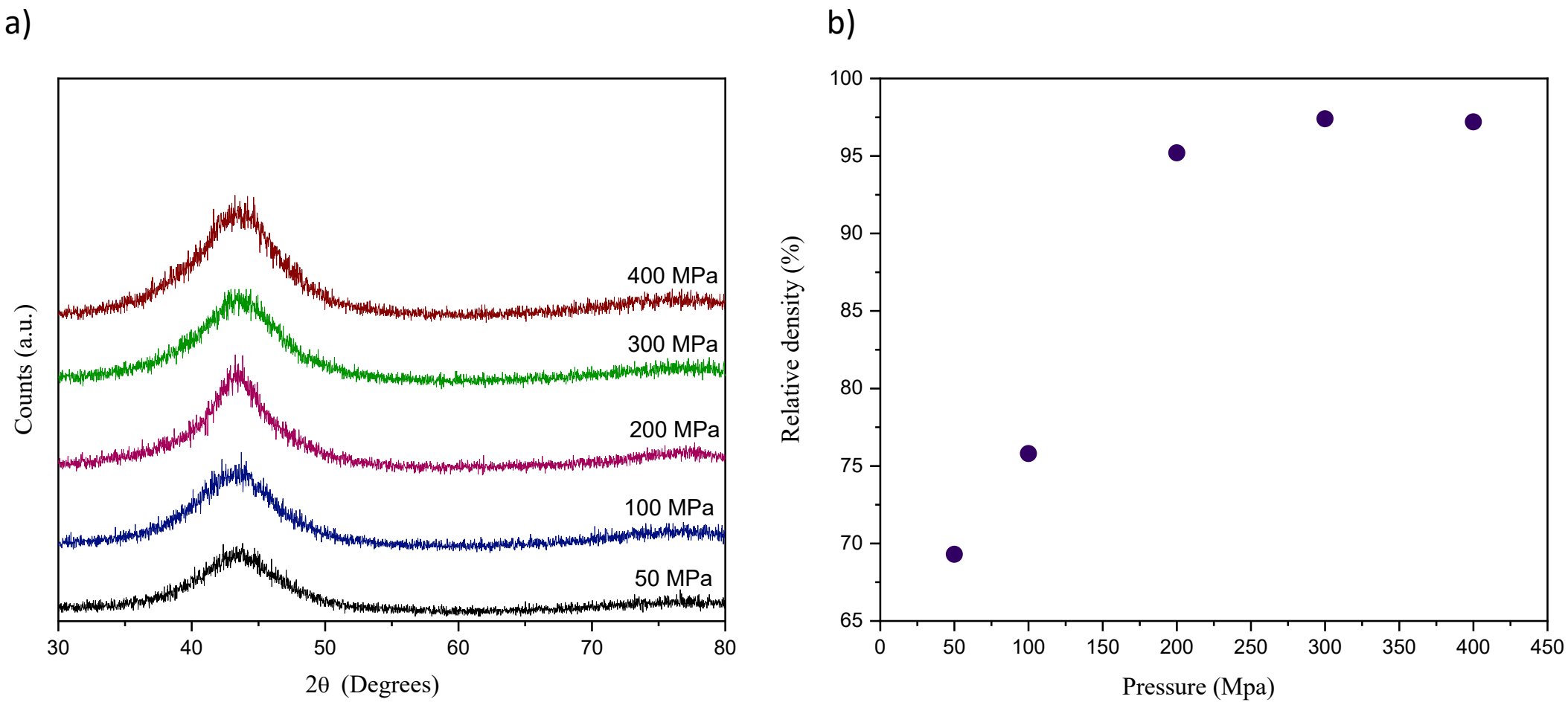

Figure 5. a) Difractogramas and b) Graph of relative density of Fe-base BMG sintered at 560 ℃ at different pressures.

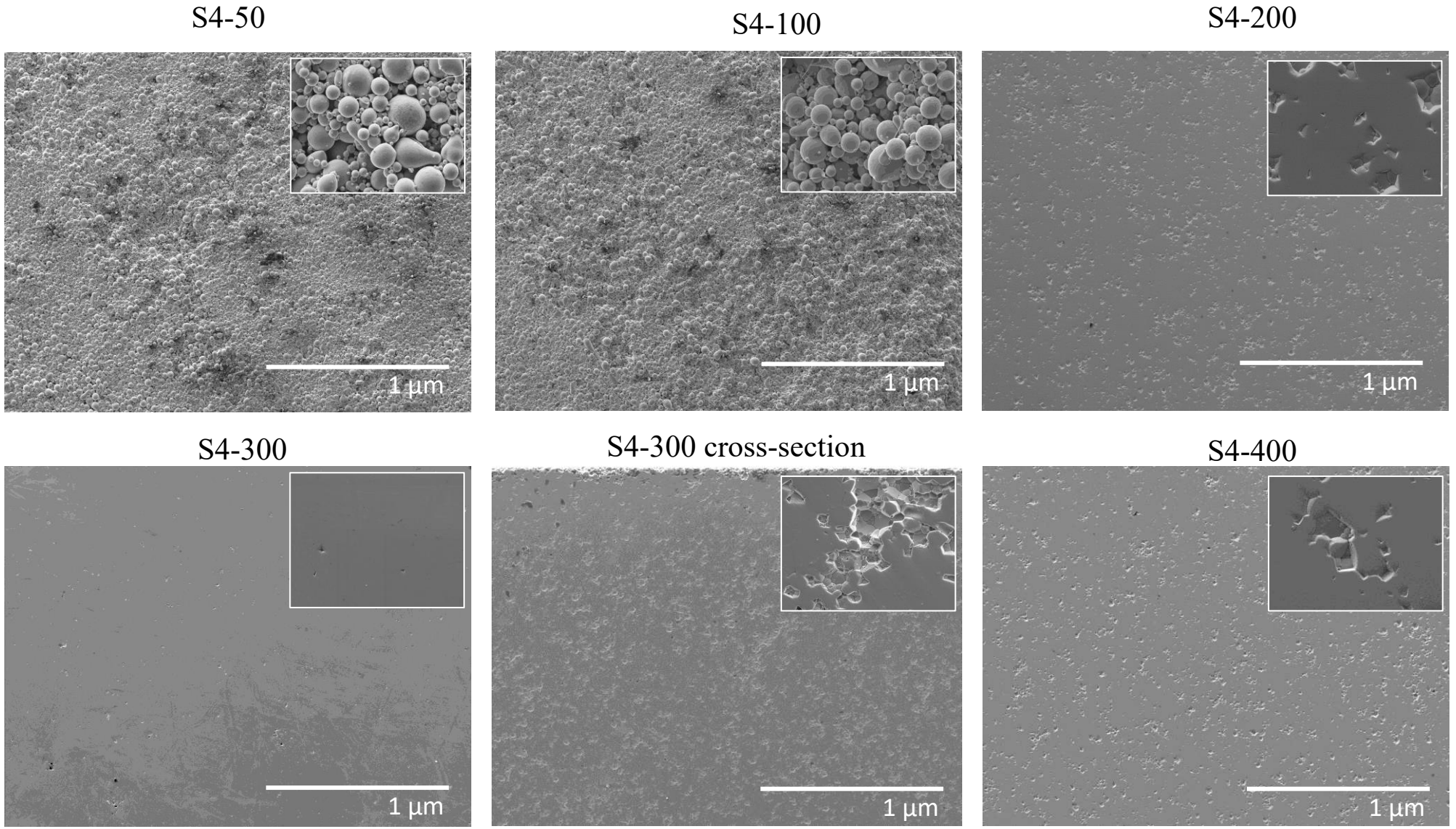

Figure 6. Top surface SEM images at the center of the sintered samples S4 at different uniaxial pressures (MPa) and cross-section of sample at 400 MPa.

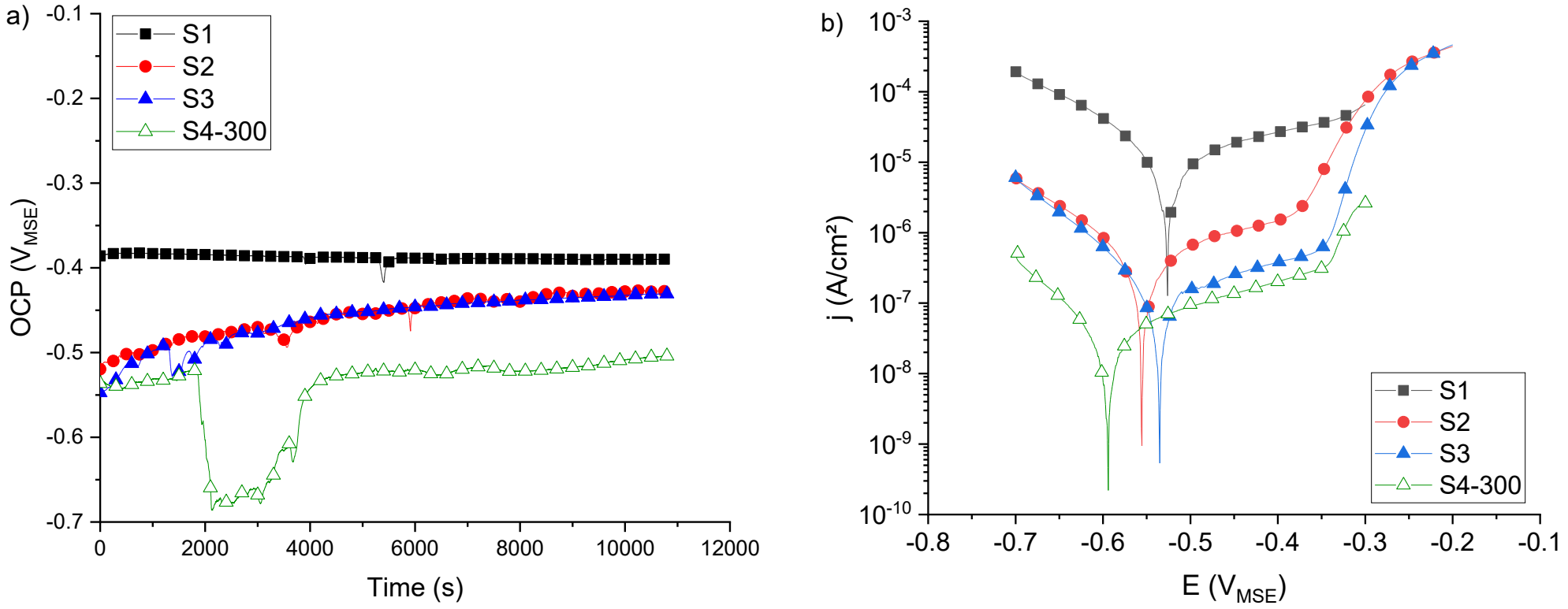

Figure 7 a) Open circuit measurements and b) linear polarization curves on S1, S2, S3, and S4-300 in 10 g/L Na_2SO_4 solution (room temperature, stagnant conditions).

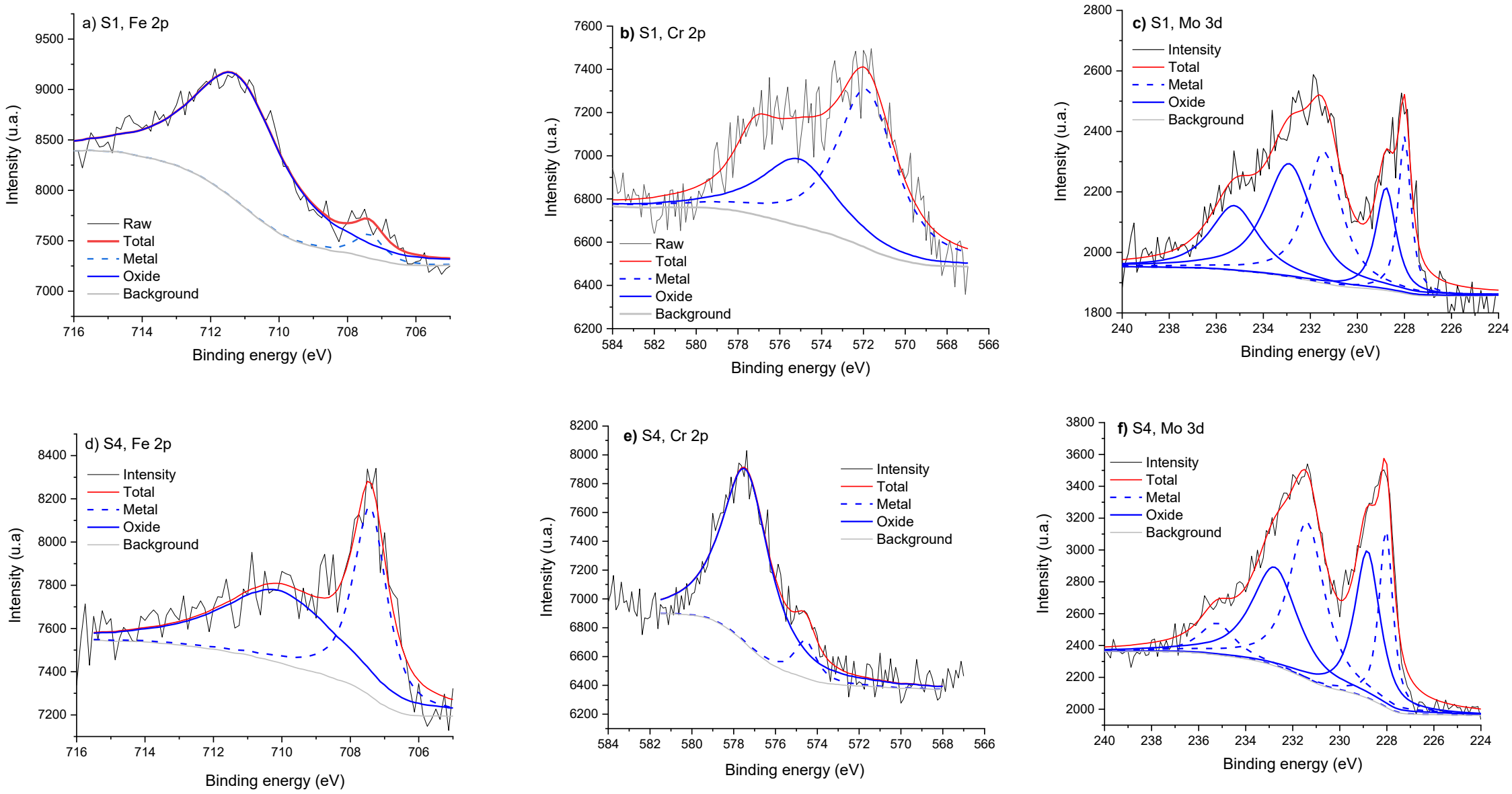

Figure 8. XPS data and fitted Fe 2p, Cr 2p, and Mo 3d spectra for (a-c) S1 and (d-f) S4.

Table 2. Tafel fit on LSV curves for the four samples immersed in a neutral sulfate solution. The equivalent weight was equal to 26.56 g/eq, and the density was taken to 7.9 g/cm^3.

Samples		**S1**	**S2**	**S3**	**S4-300**
Crystallinity (XRD)	% (± 5)	70	24	19	<1
Relative density	% (±2)	85	87	83	97
Roughness	Ra (µm) Rz (µm)	2.7 ±5.8 22.5 ±0.5	0.52 ±0.11 8.83 ±1.00	4.10 ±0.96 28.16 ±5.12	0.55 ±0.12 0.66 ±6.02
XPS	β (± 0.15)	0.47	0.60	0.72	0.82
LSV curves, Tafel plots					
Samples		**S1**	**S2**	**S3**	**S4-300**
E_{corr}	V_{MSE}	-0.527	-0.555	-0.535	-0.594
J_{corr}	$\times 10^{-6}$ A/cm²	10.9	0.403	0.112	0.003
Tafel coeff. βa	mV/decade	352	313	247	220
Tafel coeff. βc	mV/decade	129	133	84	96
Corrosion rate	$\times 10^{-3}$ mmpy	82.0	4.80	0.98	0.31
EIS Fits ($\chi^2/\|Z\| < 0.05$)					
Samples		**S1**	**S2**	**S3**	**S4-300**
		$R_e + Q_{sc}/(R_{ct}+W)$	$R_e + Q_{sc}/(R_{ct})$		
R_e	Ω cm²	129	65	71	52
Q_{sc}	F $s^{(n-1)}$ cm^{-2}	700 $\times 10^{-6}$	97 $\times 10^{-6}$	67 $\times 10^{-6}$	39 $\times 10^{-6}$
n	u.a.	0.60	0.80	0.82	0.78
R_t	Ω cm²	95	88 $\times 10^3$	341 $\times 10^3$	22 $\times 10^6$
σ_1	Ω $s^{1/2}$ cm²	1.06 $\times 10^3$	--	--	--
C	F cm^{-2}	23 $\times 10^{-3}$	166 $\times 10^{-6}$	133 $\times 10^{-6}$	262 $\times 10^{-6}$

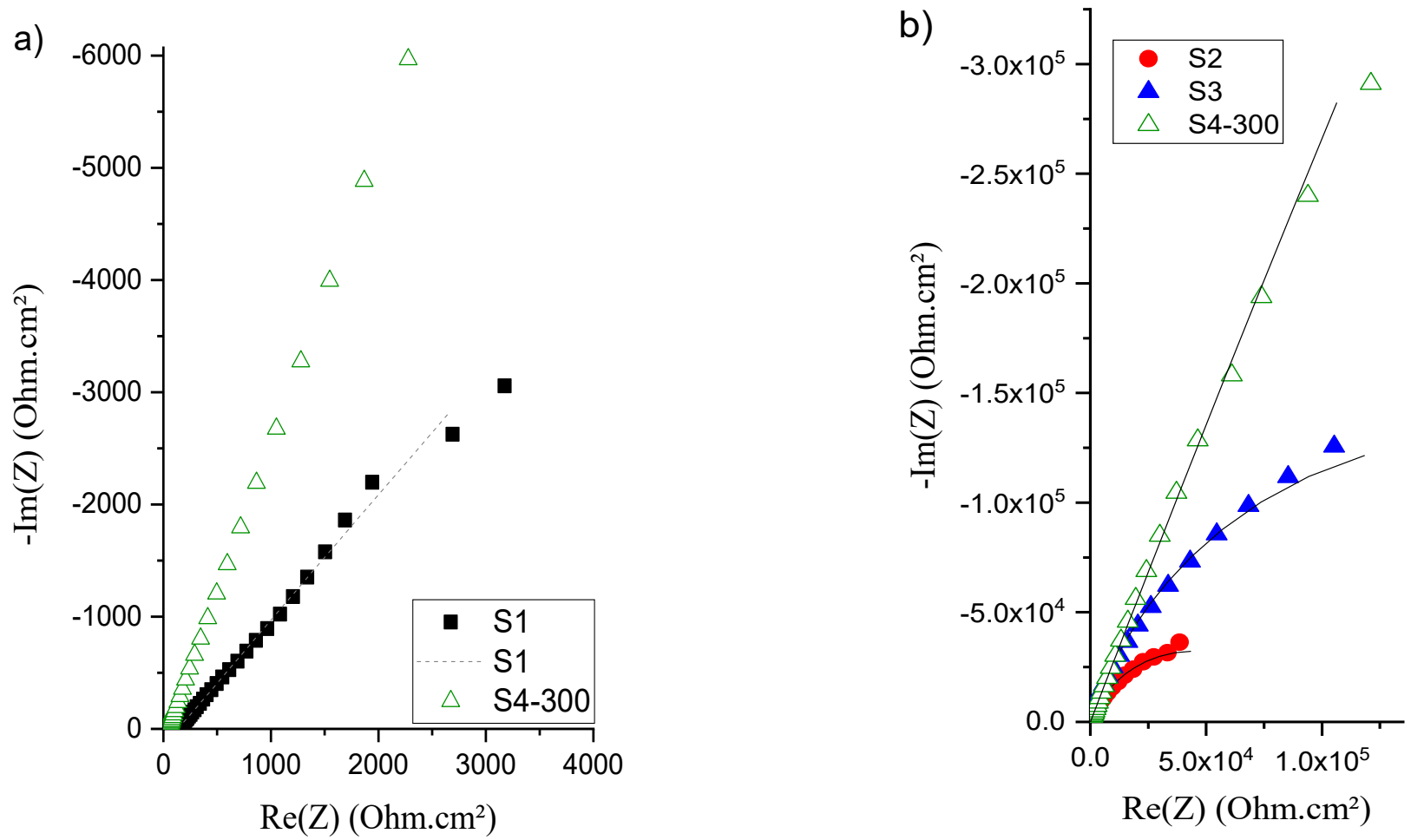

Figure 9. Nyquist diagrams on four samples immersed in an aerated, stagnant sulfate solution. a) zoom for S1 sample (high crystallinity ratio) and b) comparison between samples with low crystallinity ratio. The dash lines are the results of the EEC fits.